Artificial Intelligence

Deep Learning Segmentation, Visualization, and Automated 3D Assessment of Ciliary Body in 3D Ultrasound Biomicroscopy Images

Ahmed Tahseen Minhaz[1], Duriye Damla Sevgi[2], Sunwoo Kwak[3], Alvin Kim[4], Hao Wu[1], Richard W. Helms[5], Mahdi Bayat[6], David L. Wilson[1,7], and Faruk H. Orge[5]

[1] Department of Biomedical Engineering, Case Western Reserve University, Cleveland, OH, USA
[2] Indiana University Health, Indianapolis, IN, USA
[3] Department of Bioengineering, University of Pennsylvania, Philadelphia, PA USA
[4] Department of Mechanical Engineering, Case Western Reserve University, Cleveland, OH, USA
[5] UH CMC Division of Pediatric Ophthalmology and Adult Strabismus, Rainbow Babies and Children's Hospital, Cleveland, OH, USA
[6] Department of Electrical Engineering and Computer Science, Case Western Reserve University, Cleveland, OH, USA
[7] Department of Radiology, Case Western Reserve University, Cleveland, OH, USA

Purpose: This study aimed to develop a fully automated deep learning ciliary body segmentation and assessment approach in three-dimensional ultrasound biomicroscopy (3D-UBM) images.

Methods: Each 3D-UBM eye volume was aligned to the optic axis via multiplanar reformatting. Ciliary muscle and processes were manually annotated, and Deeplab-v3+ models with different loss functions were trained to segment the ciliary body (ciliary muscle and processes) in both en face and radial images.

Results: We trained and tested the models on 4320 radial and 3864 en face images from 12 cadaver eye volumes. Deep learning models trained on radial images with Dice loss achieved the highest mean F1-score (0.89) for ciliary body segmentation. For three-class segmentation (ciliary muscle, processes, and background), radial images with Dice loss achieved the highest mean F1-score (0.75 for the ciliary process and 0.82 for the ciliary muscle). Part of the ciliary muscle (10.9%) was misclassified as the ciliary process and vice versa, which occurred owing to the difficulty in differentiating the ciliary muscle–processes border, even by experts. Deep learning segmentation made further editing by experts at least seven times faster than a fully manual approach. In eight cadaver eyes, the average ciliary muscle, process, and body volumes were 56 ± 9, 43 ± 13, and 99 ± 18 mm^3, respectively. The average surface area of the ciliary muscle, process, and body were 346 ± 45, 363 ± 83, and 709 ± 80 mm^2, respectively. We performed transscleral cyclophotocoagulation in cadaver eyes to shrink the ciliary processes. Both manual and automated measurements from deep learning segmentation show a decrease in volume, surface area, and 360° cross-sectional area measurements.

Conclusions: The proposed deep learning segmentation of the ciliary body and 3D measurements showed transscleral cyclophotocoagulation-related changes in the ciliary body.

Translational Relevance: Automated ciliary body assessment using 3D-UBM has the translational potential for ophthalmic treatment planning and monitoring.

Introduction

Glaucoma, the second leading cause of blindness, is defined as damage to the optic nerve mainly owing to increased pressure (intraocular pressure [IOP]) in the eye.[1] Aqueous humor (AH), a clear fluid with a consistency similar to water, is produced constantly from the ciliary body. After being produced behind the iris, AH travels through the pupil, circulates in the anterior chamber, and drains away from the eye through openings at the iridocorneal angle. At the iridocorneal angle, a filtering meshwork (trabecular meshwork [TM]) exists, which also helps to regulate the drainage, as it forms resistance to the flow. Through the TM, AH flows into Schlemm's canal and then to the collector channels and gets absorbed into the episcleral veins. This drainage pathway represents approximately 80% of the drainage, and the remaining 20% is drained through the uveoscleral pathway.

If the drainage of AH does not match the production, or if the normal circulation is blocked because of various pathologies, there is an increase in the IOP gradient to maintain an outflow equal to the inflow. The normal range of the IOP is accepted to be 10 to 21 mm Hg; an IOP of greater than 22 mm Hg is defined as elevation. This increase in the IOP leads to irreversible damage to the optic nerve, causing glaucoma. Therefore, early detection, treatment, and follow-up are crucial to preventing blindness.

Several types of glaucoma are mainly defined by the cause of the IOP increase (e.g., inflammatory, pigment dispersion, neovascular, and secondary tumors), anatomic changes (e.g., open angle, closed angle, narrow-angle, secondary to pupil block, and traumatic), age of onset (e.g., congenital and juvenile), and other reasons affecting AH circulation.

To truly understand the mechanism of glaucoma, doctors need to visualize the ciliary body (ciliary processes and ciliary muscles), iris, pupil, lens, sulcus, anterior chamber, iridocorneal angle (and TM), Schlemm's canal, collector channels, and episcleral veins in good detail.[2–4] In congenital glaucoma, the most severe form of glaucoma, the affected babies are born with underdeveloped or malformed structures affecting the normal circulation of AH. Therefore, in many cases, understanding which part of the ocular anatomy is altered allows the appropriate surgical correction to normalize the structures or to allow bypassing the blocked areas of drainage. Unlike in adults, where the vast majority of the cases can be treated with topical and/or oral medications, the pediatric population and adult patients with advanced or complicated glaucoma are treated with surgical intervention.[5,6]

Surgical treatments for glaucoma involve angle surgeries (i.e., goniotomy and trabeculotomy) or more disruptive approaches (trabeculectomy, tube shunt, and cyclophotocoagulation [CPC]).[7] Surgical success is highly correlated with the experience and approach of the physician, timing, postoperative care, and the wound-healing process of the individuals. However, anatomic variations in the patients' eyes inevitably affect the outcome immensely, and many studies have failed to show surgical success with underlying anatomic variations.[5,8–11]

Ophthalmologists use different imaging techniques to visualize the various anatomic structures. Historically, microscopes, magnifying lenses, and mirrors have been used for direct visualization of the structures. These techniques are readily available in every ophthalmic practice and hence widely used, but are limited by their potential subjectivity, patient cooperation, experience of the examiner, inability to see behind the iris and through the sclera, and limited capturing techniques.[12]

Objective assessment of the anterior segment is enabled by imaging modalities such as ultrasound biomicroscopy (UBM) and anterior segment optical coherence tomography. UBM has been used to quantitatively assess tissue structures important in the development, mechanistic analyses, and the treatment of glaucoma.[13–15] Anterior segment optical coherence tomography is noncontact and has a higher resolution than UBM. However, it is expensive and has limited ability to image structures posterior to the iris, that is, the ciliary body, because the iris is opaque to light. Optical coherence tomography also cannot be used in the case of disease or injury causing increased opacity in the eye.[14] According to He et al.,[13] the major contribution of UBM is in glaucoma diagnosis, staging, and surgeries.

Studies on assessing the ciliary body in the literature are either qualitative or only focus on the two-dimensional (2D) distance-based biometrics of the tissue, which is not automated, time consuming, and observer dependent.[2–4,16] Ku et al.[3] showed that patients with a large ciliary body had an increased likelihood of having angle-closure glaucoma. Wang et al.[4] compared the structural differences of the ciliary body in eyes with and without malignant glaucoma using several point-to-point distance measures on the ciliary body, such as the maximum thickness, thickness at the point of the scleral spur, 1000 μm from the scleral spur, anterior placement of the ciliary body, and trabecular–ciliary process angle. They found that the ciliary body was anteriorly rotated

and decreased in thickness in eyes with primary angle closure.[4] Moreover, they stated the need for studies to "elucidate the relationship between ciliary body parameters and the mechanism of primary-angle closure." Safwat et al.[16] showed a decrease in the IOP and morphological change in the ciliary body (decrease in length-based metrics) after CPC, where part of the ciliary body shrinks owing to laser application. Besides glaucoma, the ciliary body is important in the study of lens accommodation. Accommodation is the process through which a lens can adjust its focus from distant to near objects (and vice versa) using ciliary muscle contraction (and expansion). Pardue et al.[17] confirmed age-related changes in the ciliary body. Another study explored the quantitative measurements of ciliary muscle during accommodation only using UBM images and argued that "UBM … allowed reliable, objective, quantitative measurements of the accommodative intraocular biometric changes."[18] These important retrospective 2D studies, requiring the saving of optimal 2D-UBM views, would be much easier and more accurate than three-dimensional (3D)-UBM providing all views.

Three-dimensional UBM enables unique visualization and quantification of anterior segment structures invisible to light, such as the ciliary muscle and ciliary processes. Clinical 2D-UBM systems are inexpensive, available, and reimbursed in the United States, but they are underused owing to the lack of clinical expertise and a dedicated ultrasound operator. Limitations lie in the visualization of the whole anterior segment and accurate measurements of these landmark-based biometrics, because these depend on the ultrasound operator's expertise to properly align the probe and manually locate landmarks.[13,19] Qureshi et al.[19] measured ciliary body biometrics (i.e., ciliary body thickness, area, length, and ciliary body–iris contact distance) from UBM images and found poor agreement between observers. Li et al.[20] measured similar ciliary body biometrics with transverse images (as opposed to longitudinal images) and showed good intraobserver reliability and interobserver agreement. They concluded that conventional longitudinal images cannot capture the ciliary processes folds and leads to poor agreement between observers. Although biometrics from transverse images provide better agreement, they are not capable of providing anatomic information of the ciliary body relative to other structures. With 3D-UBM, images are acquired by a nonspecialist and interpreted intuitively. With interactive digital slicing of a 3D-UBM volume, one can position planes for accurate 2D biometric measurements. In addition, 3D-UBM allows both en face and conventional 2D views alongside unique 3D visualization and measure-ments of 3D biometrics, enabling a whole 360° anterior segment evaluation, which is not possible by the current clinical practice of 2D-UBM, because the ultrasound operator takes images at a few selected orientations.

Semantic segmentation is the task of classifying each pixel (voxel) in an image into a particular set of classes. Segmentation of the ciliary body tissues, such as ciliary muscle and ciliary processes in 3D-UBM volume, enables intuitive visualization and measurements of the tissue not possible via a manual approach. Deep learning–based approaches have been very popular and applied successfully in different tasks in the medical image domain, namely, image reconstruction, anomaly detection, classification, and semantic segmentation of organs.[21–24] For a specific task, deep learning networks learn from examples and may be used to perform the same task on an unseen dataset. Therefore, a trained deep learning segmentation network can predict the ciliary body (muscle and processes) in 3D-UBM volumes.

In this study, we proposed a new method for the visualization, segmentation, and 3D measurement of the ciliary body with 3D-UBM. This process includes acquiring 3D volume visualizations of the anterior chamber and the ciliary body, creating radial and en face views of the ciliary body, segmenting the ciliary body using a deep learning method, and creating 3D measurements. We evaluated the segmentation method, and automated measurements are compared against manual measurements. To our knowledge, this publication is the first focusing on the segmentation of the ciliary body and automated measurements.

Methods

The 3D-UBM System

We created a 3D-UBM imaging system using a conventional high-frequency (50 MHz) 2D-UBM probe.[25] Figure 1 shows the design of the 3D-UBM system. A motorized stage moves the ultrasound probe across the eye to capture the 3D volume of the anterior segment. The system is attached to a surgical microscope for precise placement above the eye. A thin plastic layer filled with water (ClearScan) is applied to the eye, which acts as an acoustically invisible layer between the probe and the eye. We developed software that coordinates the motor and probe movements and image acquisition. Each 3D volume consists of 1000 sagittal images acquired along the x-axis across an approximately 16-mm anterior segment. Each volume is of size 1000 × 384 × 2048, with a physical dimension of approximately 16 mm × 16 mm × 10 mm. Each
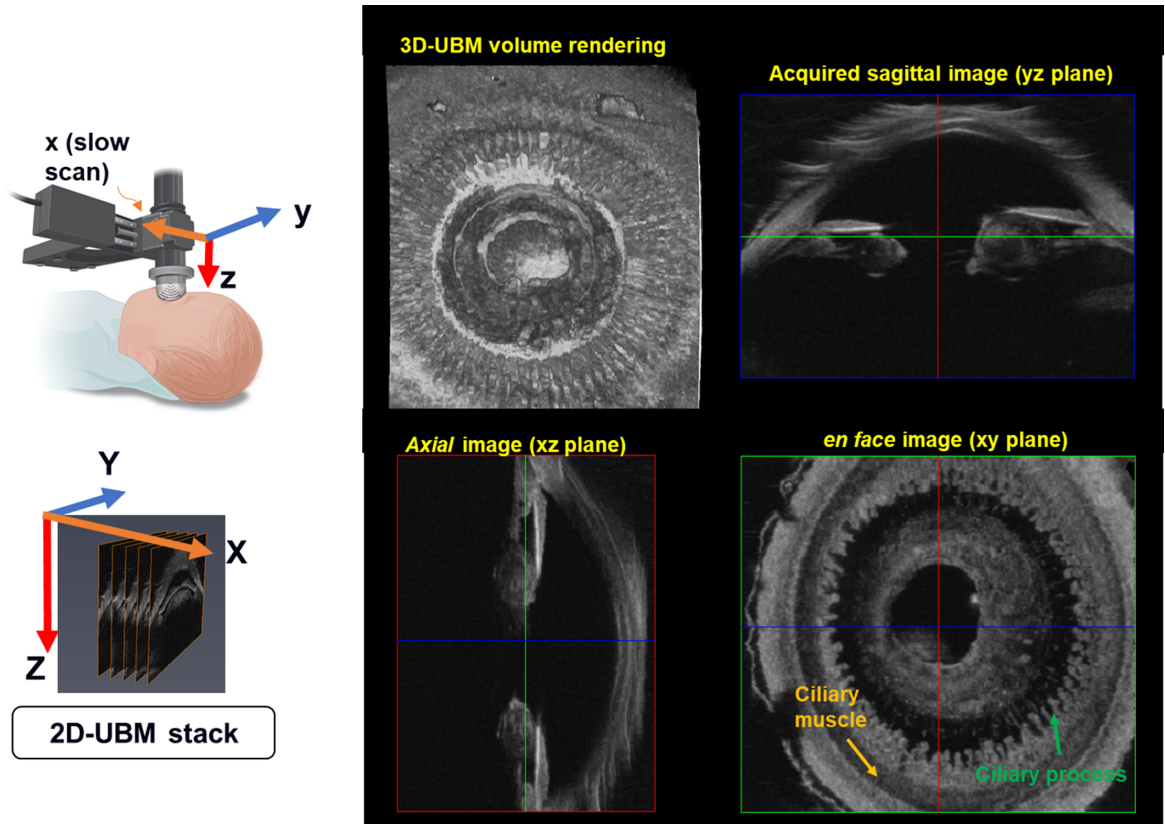
Figure 1.   A 3D-UBM system and images of ciliary body tissues. The 2D-UBM probe is translated across the eye using a motorized stage and surgical microscope to acquire a 2D image (yz plane) stack along the slow-scan direction (x-axis). From the acquired rendered volume, sagittal image (yz), axial image (xz), and en face image (xy) of the ciliary muscle and ciliary processes can be visualized clearly.

volume scan consisting of 1000 sagittal images takes approximately 100 seconds.

Image Preprocessing

Our approach to automated measurements of the ciliary body using 3D-UBM starts with image preprocessing, which includes optic axis alignment of the entire volume and extraction of en face and rotational images.

Each 3D-UBM volume was aligned to make sure the coronal plane is perpendicular to the optic axis (Fig. 2). We used Amira (ThermoFisher Scientific, Waltham, MA) to first semiautomatically find the plane, which is perpendicular to the optic axis of the eye. We resampled the volume based on that plane geometry. After optic axis alignment, the ciliary muscle and processes are visible in the same en face view, decreasing the effort during manual segmentation. We used a voxel size of 0.05 mm × 0.05 mm × 0.05 mm to resample the volume to make an isotropic volume $V(x, y, z)$. En face images (xy images) can be obtained directly from the volume.
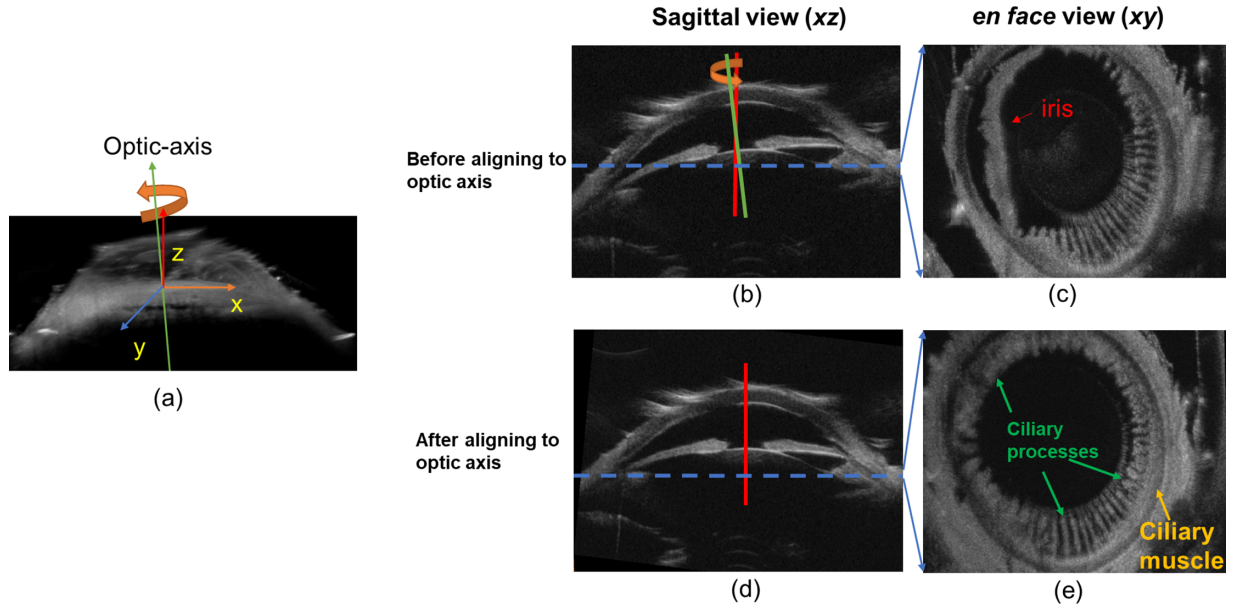
To create radial images, we performed multiplanar reformatting on data along the optic axis with the pupil as the center. Each 2D radial image is expressed as $I_\theta(r,z)$, where z and r are the axis and radii of the radial image data, respectively, and θ is the rotating angle along the z-axis with the pupil as the center. The yz plane is rotated anticlockwise at a specific angle interval, and the coordinates of the $I_\theta(r,z)$ are extracted using the following formula:

$$\begin{cases} x = r\cos\theta \\ y = r\sin\theta \\ z = z \end{cases}$$

We interpolated each radial image $I_\theta(r,z)$ data from the 3D volume V using trilinear sampling and obtained radial images, as shown in Supplementary Figure S1.

Deep Learning Segmentation of the Ciliary Body

We performed deep learning semantic segmentation of the ciliary body (muscle and processes) on

Sagittal view (*xz*)

***en face* view (*xy*)**

Before aligning to optic axis

(b)

(c)

After aligning to optic axis

(d)

(e)

Figure 2. Alignment of the 3D-UBM volume to the optic axis. (a) Direction convention used in 3D-UBM; (b) before resampling, the *z*-axis is not parallel to the optic axis (*green line*); (c) misaligned en face view contains parts of the iris; (d) sagittal view after aligning volume to the optic axis; and (e) correctly aligned en face view of the ciliary body, which contains ciliary muscle and processes.
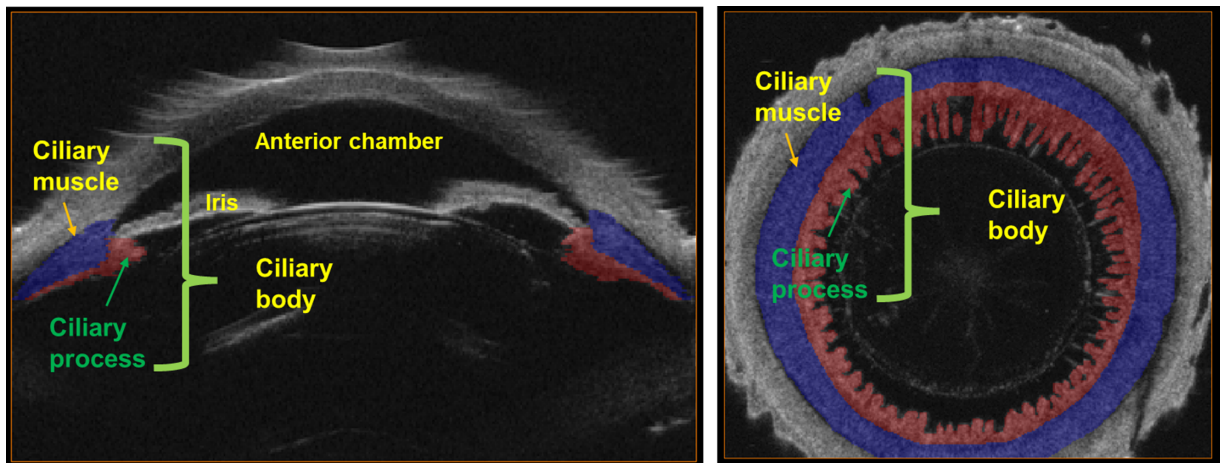
Figure 3. Segmentation of ocular structures in the anterior segment of the eye. *Green*, anterior chamber; *purple*, iris; *blue*, ciliary muscle; *red*, ciliary processes. Ciliary muscle and ciliary processes together are called the ciliary body. Experts perform manual annotation by looking at the ciliary body in 3D. From manual annotation, 3D volumetric and area measurements of ciliary muscle and processes can be made.

the resampled en face and radial images (Fig. 3). En face images show a better distinction between the ciliary muscle and the ciliary processes, which is why we used the en face plane to create ground truth annotations and other planes for verification. We used the Deeplab-v3+ model for training our segmentation model.[26] A detailed schematic of the deep learning segmentation model is shown in Figure 4. Deeplab-v3+ contains an encoder–decoder architecture, where the encoder aggregates discriminative features at multiple scales, and the decoder gener-

ates a dense semantic segmentation mask using the high-dimensional features obtained by the encoder. The encoder in Deeplab-v3+ contains a backbone network (i.e., Resnet) pretrained on ImageNet and is used for extracting features. A wider receptive field (field of view) leads to better semantic segmentation. In addition to convolution blocks, Deeplab-v3+ uses atrous convolution in the last few blocks of the encoder, which increases the receptive field (or field of view) without adding any computational cost. Deeplab-v3+ also contains an atrous spatial pyramid pooling module
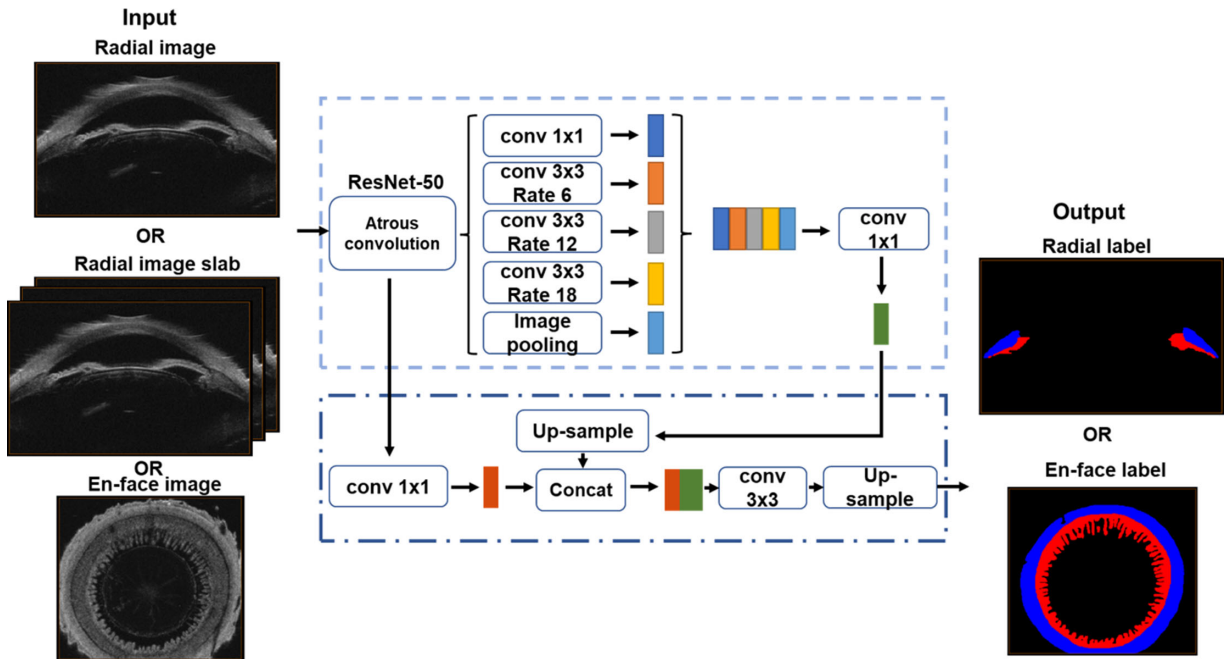
Figure 4. Deep learning convolution neural network (Deeplab-v3+) architecture for the semantic segmentation of the ciliary body. In the output-labeled image, the *red area* is the ciliary process, *blue* is the ciliary muscle, and *black* is the background. For two-class segmentation, the ciliary muscle and body are lumped together and noted as the ciliary body.

that uses atrous convolution at three dilation rates (6, 12, and 18) to obtain multiscale semantic contextual information. The decoder is used to restore the edge information and resolution of the feature map to obtain the final semantic segmentation mask. By using these novel structures, Deeplab-v3+ produces accurate semantic segmentation results among different datasets.

We created two-class and three-class ciliary tissue segmentation models. For two-class segmentation, the model creates a probability map for the ciliary body and background. For the three-class segmentation, the model creates a probability map for the ciliary muscle, ciliary processes, and background. The models were trained on two different loss functions: weighted cross-entropy (WCE) and Dice loss. Losses in models were minimized using an adaptive moment estimation optimizer and weights within the model were updated. Once training was completed, test en face and radial images were provided to the network as inputs. The network creates a probability map for the image. Each pixel is assigned the class that has the highest probability.

Biometrics Measurements of the Ciliary Body

After segmentation of the ciliary body (muscle and processes), we calculated unique 3D measurements of the ciliary body. From the ground truth annotations and automated segmentation, we measured the volume of the ciliary body, ciliary muscle, and ciliary processes. Ciliary processes increase the surface area by adding folds to allow more fluid production.[26] We measured the number of ciliary processes, surface area of the ciliary processes, muscle, and body. We computed the cross-sectional ciliary body area in each radial slice, giving us a 360° map of area metrics. We also measured 2D biometrics (i.e., ciliary muscle thickness and ciliary processes length) following the approach suggested by Li et al.[20] However, whereas their approach computed these biometrics based on a small visible portion of the ciliary body, our approach computes these biometrics over entire 360° of the anterior segment.

Dataset

We acquired a total of 12 eye volumes from 8 cadaver eyes using our 3D-UBM system. Four cadaver eyes from two donors (a 67-year-old man and a 58-year-old woman) were purchased from Tissue for Research Ltd. The other four cadaver eyes were acquired from an eye bank and were scanned before and after overlapping circumferential applications of transscleral CPC (TS-CPC). In TS-CPC, a diode laser probe is placed on the anterior border of the limbus, and a laser is applied to shrink the ciliary tissue.

A diode laser probe (G-probe, IRIDEX, Mountain View, CA) was positioned parallel to the optic axis to perform TS-CPC, and the laser was delivered at 2000 mW power for 2.5 seconds between 12 o'clock and 6 o'clock of the eye successively covering 180°. Cadaver eyes were placed in a 3D-printed eye holder apparatus for scanning. All data are provided by the Division of Pediatric Ophthalmology and Adult Strabismus, Rainbow Babies and Children's Hospital. To perform labor-intensive, accurate manual segmentation of ciliary processes and muscles, images were segmented by two trained undergraduate students and reviewed, and sometimes edited, by a senior PhD student and ophthalmology resident. The initial trainer and final arbiter on segmentation was an ophthalmology specialist (F.H.O.), with 18 years of experience in pediatric ophthalmology, which included regular imaging of anterior segment structures with UBM. For the two-class segmentation (ciliary body and background), ciliary muscle and ciliary process labels were added to create a new label: ciliary body. Region filling was used to fill any hole within the label. We generated both en face and radial images of the ciliary muscle and processes from the eye volumes. From each volume, 360 radial images are generated at 0.5° intervals, as described in the Methods. Radial image data consist of 4320 (12 volumes × 360 images per volume) images. The number of en face images generated from 3D volumes was 3864 (12 volumes × 322 images per volume) for comparison.

Deep Learning Network Training and Performance Evaluation

We used three types of images to train the segmentation networks: en face, radial, and radial image slab (radial images and adjacent ±1 slice). The input size for training images was 256 × 352 pixels (0.0455 mm × 0.043 mm) to ensure near isotropic pixels in both directions, while maintaining height and width as a factor of 2^N ($N = 4$). We performed data augmentation, that is, random rotation, reflection, scaling, translation, and random adjustment of brightness, and contrast on our training data to make the model robust and prevent overfitting.

We optimized the deep learning segmentation models using the adaptive moment estimation optimizer.[27] We set the initial learning rate, learning rate factor, drop factor, and drop period empirically at 0.0001, 10, 0.2, and 5, respectively. Transfer learning was used to train the segmentation model. A ResNet-50 model pretrained on ImageNet was used as a backbone for the Deeplab-v3+ encoder networks. The models

were fine tuned using the combination of a small initial learning rate (0.0001) and a high learning rate factor (10) for the new layers, which ensured a faster learning process for the new layers than the transferred layers. We trained models using two loss functions: WCE and generalized Dice loss over the softmax outputs. The maximum number of epochs was set to 100. If the validation loss did not improve in five consecutive epochs (drop period), the learning rate was dropped by the drop factor (0.2). Early stopping was used if validation loss did not improve for 10 successive epochs. This was performed to prevent overfitting. Models with the lowest validation loss were saved. All images were processed using Amira (ThermoFisher Scientific) and MATLAB (R2020b, MathWorks, Inc., Natick, MA) on an NVIDIA GeForce GTX 1080Ti GPU (11 GB RAM).

We performed leave-one-eye-out cross-validation, where each model was trained on all images, except images from one eye that was left for testing. Evaluation metrics were calculated on images from the left-out eye. This training and testing processes were repeated eight times with the eight cadaver eyes. Each model was discarded after training, and the models did not share any parameters between themselves. Finally, performance metrics from all eight models were averaged to show the mean and standard deviation of the overall performance metrics. Network performance was quantitatively evaluated using traditional metrics, for example, accuracy, sensitivity, specificity, precision, and F1-SCORE defined as below:

$$Accuracy = (TP + TN) / (TP + TN + FP + FN) \quad (1)$$

$$Sensitivity = TP / (TP + FN) \quad (2)$$

$$Specificity = TN / (TN + FP) \quad (3)$$

$$Precision = TP / (TP + FP) \quad (4)$$

$$F1 - score = 2TP / (2TP + FP + FN) \quad (5)$$

where TP, FP, TN, and FN stand for true positive, false positive, true negative, and false negative, respectively. The F1-score is a harmonic mean of precision and sensitivity. For two-class classifications, the F1-score is the same as the Dice coefficient. For the three-class segmentation, we showed confusion matrices to illustrate prediction performance.

Results

We compared the performance of segmentation models on two image inputs for the two-class segmentation (ciliary body and background) to find the best input and loss function combination. Table 1 shows the performance of the two-class segmentation model with different image inputs and loss functions (Dice loss and WCE). Radial images with Dice loss achieved the highest mean F1-score (0.8932) and mean precision (0.8953). In direct comparison, Deeplab-v3+ models trained with Dice loss outperformed models trained with WCE. Models trained with two added sequential radial slices did not perform better than models trained with only single 2D radial images. Figure 5 shows the segmentation performance of the Deeplab-v3+ model

trained with 2D radial images as inputs and Dice loss on sample test images. In the test images, error mostly occurs at the boundary.

We evaluated the effects of analyst variability on deep learning model training. Owing to the manual effort involved, no eye was annotated by two experts. To analyze analyst variability, we compared deep learning results on eyes labeled by specific analysts. In the two-class segmentation performance evaluation using leave one-eye out cross-validation (Table 1), each eye was in the test set once while the other eyes were in the training set. When eyes annotated by expert 1 were in the test sets, the mean Dice score was 0.8949 ± 0.0335. When eyes annotated by expert 2 were in the test sets, the mean Dice score was 0.8907 ± 0.0217. The very small difference in Dice scores ($<0.51\%$) showed that

Table 1. Comparison of the Ciliary Body Segmentation Using Different Image Inputs and Loss Functions

Input Image	Loss Function	Accuracy	Sensitivity (How Much of Actual CB is Predicted)	Specificity	Precision (How Much of Predicted CB is Actually CB)	Dice Coefficient (F1-Score)
En face	WCE	0.9851 ± 0.0024	0.9314 ± 0.0256	0.9875 ± 0.0026	0.7760 ± 0.0279	0.8461 ± 0.0139
Radial	WCE	0.9902 ± 0.0013	$\mathbf{0.9759 \pm 0.0113}$	0.9906 ± 0.0012	0.7619 ± 0.0290	0.8555 ± 0.0196
Radial slice slab (3 slices)	WCE	0.9851 ± 0.0023	0.9239 ± 0.0430	0.9871 ± 0.0016	0.6874 ± 0.0316	0.7878 ± 0.0292
Radial	Dice	$\mathbf{0.9937 \pm 0.0013}$	0.8917 ± 0.0369	0.9968 ± 0.0007	0.8953 ± 0.0249	$\mathbf{0.8932 \pm 0.0253}$
Radial slice slab (3 slices)	Dice	0.9880 ± 0.0025	0.8055 ± 0.0563	0.9937 ± 0.0013	0.7973 ± 0.0325	0.8007 ± 0.0382

Generally, performance is improved when using radial images rather than en face image inputs. The best performance (highest sensitivity and Dice coefficient) using Deeplab-v3+ was achieved using radial images and Dice loss. Adding adjacent slices (image $\pm$ 1 slice to create a radial slice slab) did not improve segmentation performance. Values presented in bold represent the highest mean performance metrics.
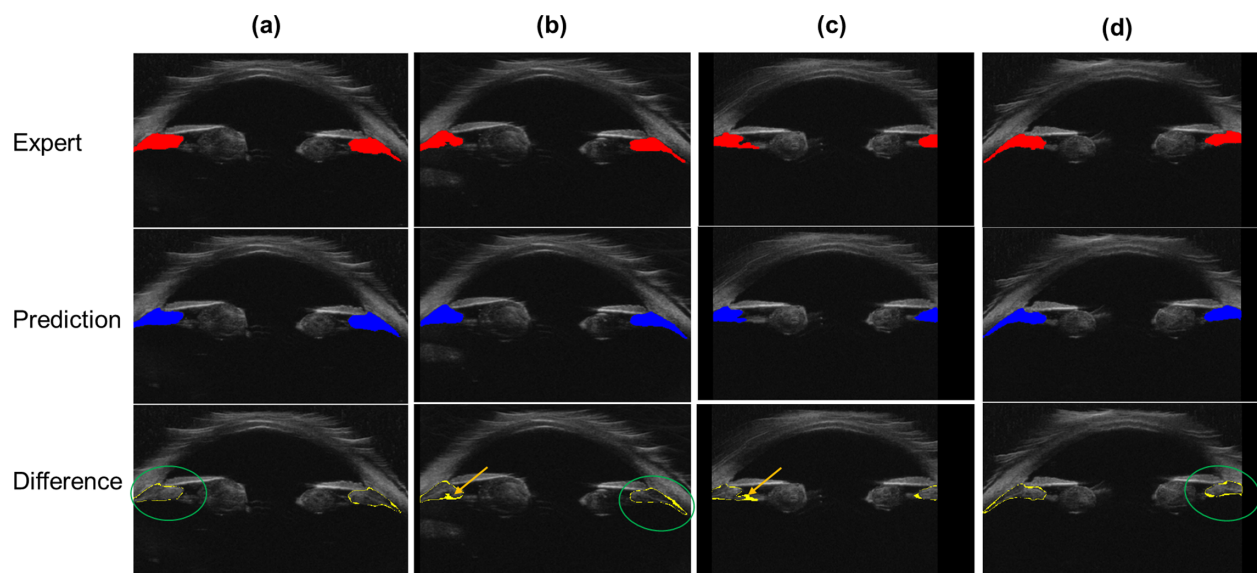
Figure 5. Deep learning segmentation of the ciliary body. All four panels (a)–(d) show expert annotation of the ciliary body, prediction from deep learning segmentation, and the difference (*top to bottom*). Areas with *yellow arrows* show incorrect segmentation of the ciliary body. Areas with a *green oval* indicate possible ciliary body location that might have been missed by experts.

Table 2. Comparison of the Three-Class Segmentation of Ciliary Body Tissues Using Different Image Formats and Loss Functions

Input Type + Loss Function	Loss Function	Metrics	Background	Ciliary Process	Ciliary Muscle
Radial	Dice	Sensitivity (%)	0.9965 ± 0.0009	0.7471 ± 0.0837	0.8311 ± 0.1158
		Specificity (%)	0.8853 ± 0.0507	0.9961 ± 0.0015	0.9973 ± 0.0010
		Precision (%)	0.9965 ± 0.0015	0.7596 ± 0.0866	0.8158 ± 0.0582
		F1-score (%)	**0.9965 ± 0.0008**	**0.7487 ± 0.0573**	**0.8173 ± 0.0568**
Radial slice slab (3 slices)	Dice	Sensitivity (%)	0.9963 ± 0.0012	0.7385 ± 0.0854	0.8273 ± 0.1094
		Specificity (%)	0.8834 ± 0.0447	0.9959 ± 0.0017	0.9972 ± 0.0013
		Precision (%)	0.9964 ± 0.0013	0.7511 ± 0.0935	0.8085 ± 0.0723
		F1-score (%)	0.9963 ± 0.0008	0.7390 ± 0.0565	0.8113 ± 0.0554
En face	WCE	Sensitivity (%)	0.9818 ± 0.0021	0.7979 ± 0.0714	0.8751 ± 0.0979
		Specificity (%)	0.9460 ± 0.0240	0.9902 ± 0.0033	0.9870 ± 0.0029
		Precision (%)	0.9975 ± 0.0011	0.6226 ± 0.0854	0.6238 ± 0.0807
		F1-score (%)	0.9896 ± 0.0010	0.6935 ± 0.0505	0.7227 ± 0.0614

Similar to two-class segmentation, radial images as inputs perform better than en face image inputs. The highest precision and F1-score (Dice coefficient) in the Deeplab-v3+ model are achieved using radial images as inputs and Dice loss and loss function. Adding adjacent slices (image $\pm$ 1 slice to create a radial slice slab) did not improve segmentation performance.

there were no consistent differences between analysts in labeling.

Table 2 shows three-class segmentation (ciliary muscle, processes, and background) performance in Deeplab-v3+ models with different image inputs and loss functions. Models trained with 2D radial images and Dice loss outperform other models in terms of the mean F1-score (0.8173). Similar to two-class segmenta-tion, adding sequential radial slices did not improve the segmentation performance. Figure 6 shows the three-class segmentation of sample test 2D radial images using the best-performing model. In some areas, the ciliary muscle was misclassified as ciliary processes and vice versa. The boundary between the ciliary muscle and processes is often challenging to distinguish in some cases, even by trained experts. Table 3 shows
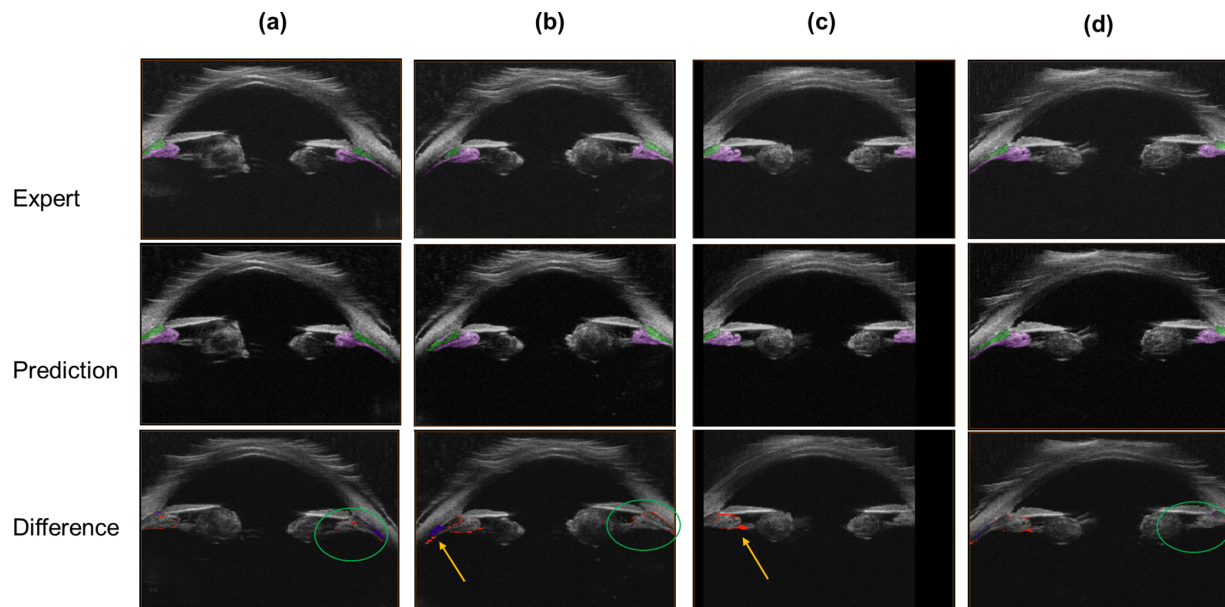
Figure 6. Deep learning segmentation of the ciliary muscle and ciliary processes. Panels (a)–(d) show expert annotation of the ciliary muscle (*green*) and ciliary processes (*purple*), prediction from deep learning segmentation, and difference (*top to bottom*). Areas with *yellow arrows* show incorrect segmentation of tissues, and areas with *green ovals* indicate possible volumes that might have been missed by experts. Predicted labels are smoother possibly because interpolation and small discontinuities in ground truth are not maintained.

Table 3. Confusion Matrix for the Three-Class Segmentation of the Ciliary Muscle, Processes, and Background Using Radial Images as Input and Dice Loss

	Predicted Background	Predicted Ciliary Processes	Predicted Ciliary Muscle
Actual background	0.9963	0.0026	0.0011
Actual ciliary processes	0.1553	0.7398	0.1049
Actual ciliary muscle	0.0704	0.1092	0.8205

Part of the ciliary processes (approximately 10%) is predicted as ciliary muscle and vice versa. Some of this misprediction can be attributed to the border between the muscle and processes being difficult to segment and intrareader variability.

Table 4. Comparison of the Measurements of the Ciliary Body Volume Between Manual Annotation and Deep Learning Segmentation Approach

	TS-CPC	Ciliary Body Volume (in mm^3) From Manual Annotation	Ciliary Body Volume (in mm^3) From Deep Learning Segmentation
Eye 1	Pre	98.75	94.27
	Post	102.55	102.36
2	Pre	134.2	129.66
	Post	122.08	113.44
3	Pre	103.11	101.71
	Post	91.51	92.6
4	Pre	69.09	71.09
	Post	66.53	65.59
5	—	93.5	101.66
6	—	106.24	108.35
7	—	102.18	104.75
8	—	98.68	93.05

Paired *t*-test shows no significant difference between the mean manual ciliary body volume measurements and deep learning segmentation volume ($P = 0.5404$).

the confusion matrix for the three-class segmentation. Approximately 10% of the ciliary process was misclassified as the ciliary muscle and vice versa. In both two-class and three-class segmentations, the predicted segmentation was smoother than the ground truth segmentation.

Table 4 compares the ground truth ciliary body volume measurements with volume measurements from two-class automated deep learning segmentation. A paired *t*-test shows a *P* value of 0.5404, which indicates the absence of a significant difference in the ciliary body volume measurements between ground truth and deep learning segmentation. Although the three-class deep learning segmentation model provides a great initial estimate of the ciliary muscle and process, further editing can be made on predicted segmentation to minimize ciliary muscle–processes misclassifica-

tion. The average time to manually annotate the ciliary muscle and processes in a 3D-UBM volume is approximately 20 hours. Editing on an already segmented volume via deep learning can take approximately 2 to 3 hours, making the process at least seven times faster. Deep learning segmentation and further refinement allow unique visualization of the ciliary body and volume and area measurements of the ciliary muscle and processes (Fig. 7).

Table 5 shows the semiautomated quantitative assessment of the ciliary body structures. We measured the number of ciliary processes, ciliary process, muscle volume, and surface area from deep learning
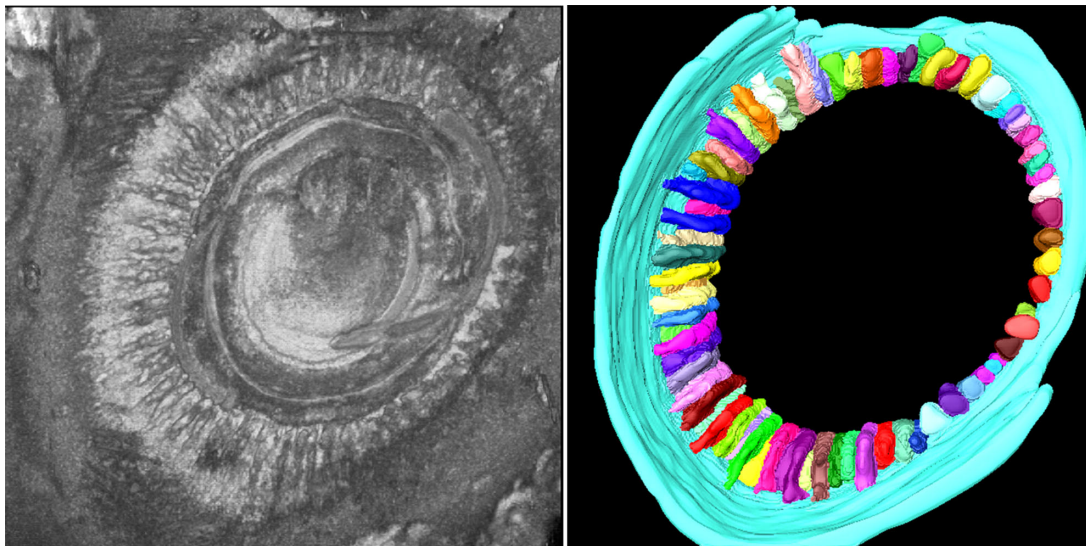

Figure 7. Visualization of ciliary muscle and processes in 3D-UBM volume. Rendering of the segmentation of the ciliary body provides unique visualization and measurements, that is, the total ciliary muscle and processes volume and surface area, number of processes, average ciliary process volume, and area.

Table 5. Quantitative Assessment of Ciliary Body Structures From Semiautomated Segmentation

| Eye	TS-CPC	No. of Processes	Volume Measurements			Surface Area Measurements			Length-Based Measurements	
			Total Volume of Ciliary Processes (mm³)	Total Volume of Ciliary Muscle (mm³)	Total Volume of Ciliary Body (mm³)	Ciliary Processes Surface Area (mm²)	Ciliary Muscle Surface Area (mm²)	Ciliary Body Surface Area (mm²)	Ciliary Muscle Thickness (mm)	Ciliary Processes Length (mm)
1	Pre	69	31.08	67.67	98.75	258.51	375.5	634.01	1.25 ± 0.30	0.88 ± 0.37
	Post		39.24	63.31	102.55	249.15	436.63	685.78	1.26 ± 0.16	0.72 ± 0.36
2	Pre	73	63.63	70.57	134.2	381.67	310.74	692.41	1.24 ± 0.13	1.25 ± 0.52
	Post		53.71	68.37	122.08	311.77	326.57	638.34	1.28 ± 0.14	1.19 ± 0.43
3	Pre	72	47.58	55.53	103.11	327.85	324.91	652.76	1.05 ± 0.11	1.10 ± 0.18
	Post		40.04	51.47	91.51	291.81	282.54	574.35	1.02 ± 0.24	1.09 ± 0.25
4	Pre	74	24.21	44.88	69.09	375.82	422.21	798.03	0.86 ± 0.19	0.65 ± 0.38
	Post		19.58	46.95	66.53	297.42	367.5	664.92	0.78 ± 0.25	0.61 ± 0.41
5		80	39.93	53.57	93.5	422.77	306.67	729.44	1.03 ± 0.16	0.76 ± 0.43
6		82	54.37	51.87	106.24	474.96	337.92	812.88	0.96 ± 0.21	0.84 ± 0.47
7		76	52.69	49.49	102.18	488.18	339.03	827.21	0.98 ± 0.17	1.08 ± 0.49
8		70	50.92	47.76	98.68	480.71	319.14	799.85	0.98 ± 0.24	0.96 ± 0.34
Mean			43.08	55.95	99.04	363.39	345.78	709.17		
SD			12.66	8.73	18.03	83.29	44.56	79.6		

Our deep learning segmentation model predicts ciliary muscle and processes, which are further refined by an expert. Segmentation of the ciliary body allows unique 3D measurements that were heretofore not possible.
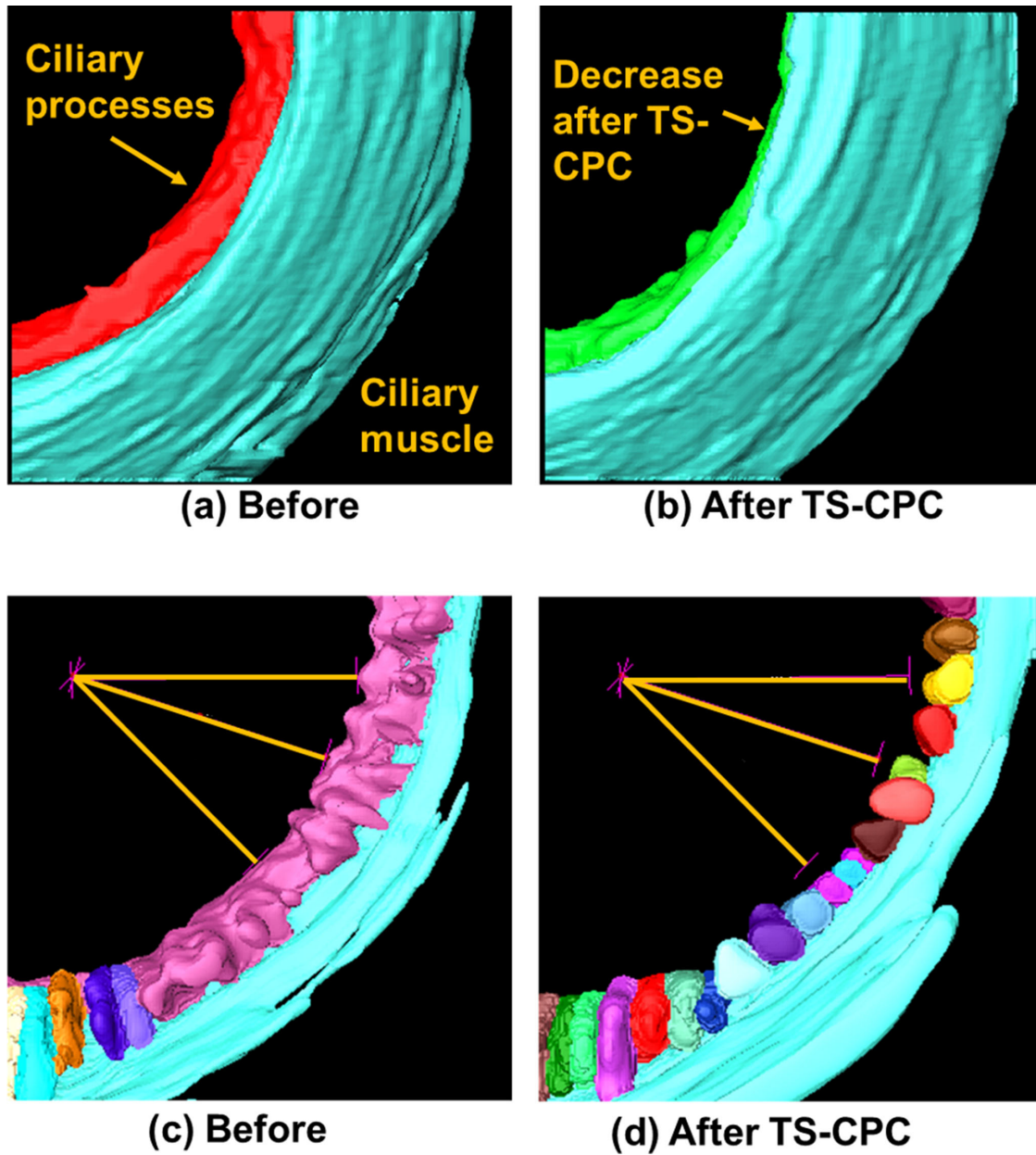
Figure 8. Ciliary body size reduction after TS-CPC treatment. Shown are renderings using semiautomated ciliary muscle and processes segmentation before (a, c) and after (b, d) TS-CPC treatments on two cadaver eyes. Shown are both anterior to posterior views of the ciliary body (a, b) and posterior to anterior views (c, d). Both eyes show a visible decrease in ciliary processes.

segmentation, followed by expert edits. In eight cadaver eyes, the average ciliary muscle, processes, and body volume were 55.95, 43.08, and 99.04 mm^3, respectively. The average surface area of the ciliary muscle, process, and body were 345.78, 363.39, and 709.17 mm^2, respectively. Table 5 also shows the length-based biometrics measurements found in the literature.[19,20] The average ciliary muscle thickness and average ciliary processes length were 1.06 and 0.93 mm, respectively.

TS-CPC was performed on four cadaver eyes using a laser diode probe for 2.5 seconds to shrink the ciliary processes. Rendering of the ciliary body shows a decrease in ciliary processes after TS-CPC on two cadaver eyes (Fig. 8). The 3D-UBM volumes before and after TS-CPC were registered, and radial lines drawn from the same point demonstrate a decrease in ciliary processes in the operated region. Changes in the ciliary process and muscle volumes were observed after TS-CPC in three of four cadaver eyes. The
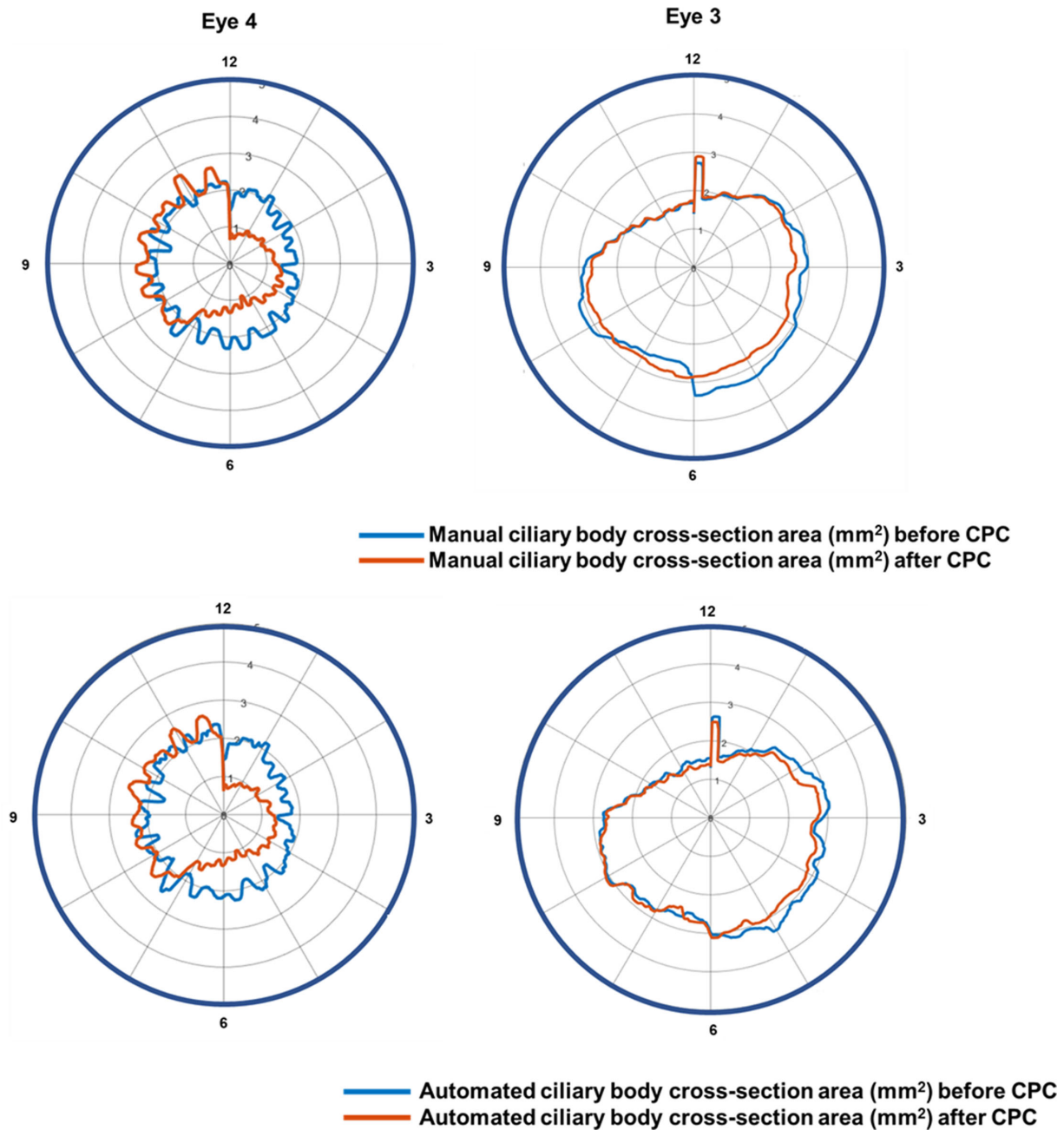
Figure 9. Comparison of manual and automated measurements of the ciliary body cross-sectional area from radial images. The 3D-UBM enables 360° 2D measurements of the ciliary body. For two cadaver eyes after CPC, 2D cross-sectional areas of the ciliary body were reduced in the location (12 o'clock to 6 o'clock) where CPC was performed.

decrease in ciliary process volume (17.6%–29.99%) was higher than that in ciliary muscle volume (5.7%–14.3%) (Supplementary Table 1 and Supplementary Figure S2).

Figure 9 shows the whole 360° cross-sectional area of the ciliary body before and after CPC using manual ground truth and automated measurements, respectively. Both measurements show shrinkage in the ciliary body after CPC. Eye 1 is considered an outlier, as

a cyst-like shape developed in one cadaver eye after applying TS-CPC (Supplementary Fig. S3).

Discussion

Results of the automated processing of the ciliary body are promising. Figures 5 and 6 demonstrate

very good segmentations of the ciliary tissue with our deep learning method. Remarkably, in some cases, deep learning correctly segmented some tissues that were missed by experts. In both two-class (ciliary body vs. background) and three-class (ciliary muscle vs. processes vs. background) models, we observed that radial images with Dice loss provided the best segmentation performance. An intuitive explanation behind the better segmentation performance using radial images is the eye's rotational symmetry, requiring fewer training images to obtain better performance using the deep learning network than using en face images. We observed no improvement when using radial slice slabs as inputs rather than simple 2D radial images. Table 4 shows no significant differences between manual and automated measurements ($P = 0.5404$) with differences of 1% to 7%.

Using 3D-UBM will enable new 3D assessments impossible with 2D. According to Li et al.,[20] they had difficulty capturing the complex 3D anatomy using their 2D biometric measurements. In eight cadaver eyes scanned, the number of ciliary processes was 75 ± 4, which agrees with literature data.[28] Table 5 shows 3D biometrics such as the mean volume of the ciliary muscle, processes, and body, and the average surface area of the ciliary muscle, process, and body. As opposed to the point-based length metrics mentioned elsewhere in this article,[19,20] these measurements are more indicative of the entire 3D anatomy of the ciliary body than point measurements from a few selected orientations. The 3D measurements do not require identifying and positioning anatomic landmarks (i.e., scleral spur) as in 2D assessments. They are also less sensitive to the angulation of the probe (tilting bias), making them more reliable and reproducible than length-based metrics. Experience with 3D-UBM suggests that we can assess biometric data on patients to evaluate changes in disease conditions, as has been done for multiple studies using 2D ultrasound examination.[29–31]

In addition to 3D biometrics, conventional 2D biometrics measurements (e.g., ciliary processes length and muscle thickness) are improved with 3D imaging (Table 5). Li et al.[20] showed good reliability in measuring ciliary processes length and muscle thickness from transverse images. However, those measurements rely on a small portion of the ciliary body and cannot capture the global ciliary body information. Their proposed measurements were also dependent on how the probe was positioned. A slight angle in positioning would reveal a different plane of the ciliary body leading to an error in length metrics. En face images from 3D-UBM after alignment with the optic axis provide the entire view of the ciliary body. Therefore,

measurements of ciliary body length and thickness (Table 5) from 3D-UBM are indicative of the entire eye, rather than a small visible area.

Our ciliary body segmentation approach includes multiple preprocessing steps that were important for reducing efforts in manual labeling and for improving deep learning segmentation and measurement performance. Preprocessing includes image alignment to the optic axis, which removes tilting bias, making it independent of how the probe was positioned for any biometric measurements.[32] Alignment brings the entire ciliary body within fewer en face planes, making the manual annotation process much easier. Initial results showed that en face and radial images performed better than did sagittal images. This finding is possibly because the ciliary body size and shape in sagittal images were constantly changing. This strategy would require a lot more images to train a deep learning model accurately. We used rotation as a data augmentation technique, which makes the model robust to any changes in alignment during testing. Therefore, even in cases of different orientations of the probe creating tilting bias in UBM images, our approach can accurately predict the ciliary body and create measurements.

We demonstrated the application of the ciliary body measurements for glaucoma treatment: TS-CPC, which is applied to destroy the ciliary body so that it does not produce enough fluid and decreases the IOP.[16] No routine imaging of these structures is performed to visualize these effects in the ciliary body after laser application. The variable effects of TS-CPC on IOP in different individuals can simply be due to tissue response, poor application of the laser, or inapplication of the laser to the intended areas. Figure 8 shows visually how ciliary processes shrunk after TS-CPC application in the operated region of two cadaver eyes. Table 5 and Supplementary Table 1 show that, after TS-CPC, ciliary muscle and processes decreased in both volume and surface area. In the operated region, changes in the ciliary muscle ranged from 5.7% to 14.3%, whereas changes in the ciliary processes ranged from 17.6% to 30.0%, which indicates that ciliary processes change faster than the ciliary muscle, which is why it was more pronounced in Figure 8. Although one cadaver eye had an increase in size, it was likely due to the formation of a cyst near the iris–ciliary body boundary. The appearance of the cyst might have altered the shape of the ciliary body and associated measurements after CPC. These automated 3D measurements and visualization of the entire ciliary body have never been conducted before, can potentially be correlated to IOP change, and may help to guide optimum treatment algorithms for the clinicians.

Our approach has some limitations. While creating ground truth annotations, analysts used the en face plane, but switched among different planes to accurately delineate the ciliary body. This process made creating ground truth annotations very time consuming and challenging. This factor limited the number of eyes that could be analyzed. Although these results were obtained on cadaver eyes, we have recently done in vivo imaging with good results after applying registration to account for small eye movements (not shown). In this preliminary report, our deep learning segmentation approach was found to be suitable for cadaver eye images. Results may be degraded if applied to another 3D ultrasound system with different image quality characteristics or possibly in vivo images from this system. Nevertheless, our demonstrated approach would likely be applicable.

In summary, automated segmentation using deep learning of 3D-UBM enables improved visualizations, automated 360° measurements, and assessment of TS-CPC treatment. Our approach shows that automated deep learning segmentation models trained on radial images with Dice loss provide the highest segmentation performance owing to the eye's radial symmetry. Automated segmentation provides comparable performance with an analyst and can be edited quickly, making the manual segmentation process much faster. Automated segmentation leads to improved visualization and automated 2D and new 3D measurements of the ciliary body that indicate a reduction in ciliary body area and volume after TS-CPC. Previously, we have shown that 3D-UBM can be used to visualize implants and devices, such as implanted intraocular lenses, a microcatheter placed in Schlemm's canal, and 360° assessments of the iridocorneal angle.[1,2] Our preliminary results suggest that the 3D-UBM and analysis methods presented herein may help to support the diagnosis of glaucoma, aid in treatment decision-making, and assess interventions.

Acknowledgments

Disclosure: **A.T. Minhaz,** None; **D.D. Sevgi,** None; **S. Kwak,** None; **A. Kim,** None; **H. Wu,** None; **R.W. Helms,** None; **M. Bayat,** None; **D.L. Wilson,** None; **F.H. Orge,** None

References

1. Cook C, Foster P. Epidemiology of glaucoma: what's new? *Can J Ophthalmol*. 2012;47(3):223–226.
2. Prata TS, Dorairaj S, De Moraes CG, et al. Is preoperative ciliary body and iris anatomical configuration a predictor of malignant glaucoma development?: Prediction of malignant glaucoma. *Clin Exp Ophthalmol*. 2013;41(6):541–545.
3. Ku JY, Nongpiur ME, Park J, et al. Qualitative evaluation of the iris and ciliary body by ultrasound biomicroscopy in subjects with angle closure. *J Glaucoma*. 2014;23(9):583–588.
4. Wang Z, Huang J, Lin J, Liang X, Cai X, Ge J. Quantitative measurements of the ciliary body in eyes with malignant glaucoma after trabeculectomy using ultrasound biomicroscopy. *Ophthalmology*. 2014;121(4):862–869.
5. Ben-Zion I, Tomkins O, Moore DB, Helveston EM. Surgical results in the management of advanced primary congenital glaucoma in a rural pediatric population. *Ophthalmology*. 2011;118(2):231–235.e1.
6. Chen TC, Chen PP, Francis BA, et al. Pediatric glaucoma surgery: a report by the American Academy of Ophthalmology. *Ophthalmology*. 2014;121(11):2107–2115.
7. Morales J, Al Shahwan S, Al Odhayb S, Al Jadaan I, Edward DP. Current surgical options for the management of pediatric glaucoma. *J Ophthalmol*. 2013;2013:1–16.
8. Mendicino ME, Lynch MG, Drack A, et al. Long-term surgical and visual outcomes in primary congenital glaucoma: 360° trabeculotomy versus goniotomy. *J Am Assoc Pediatr Ophthalmol Strabismus*. 2000;4(4):205–210.
9. Bothun ED, Guo Y, Christiansen SP, et al. Outcome of angle surgery in children with aphakic glaucoma. *J Am Assoc Pediatr Ophthalmol Strabismus*. 2010;14(3):235–239.

10. Morgan KS, Black B, Ellis FD, Helveston EM. Treatment of congenital glaucoma. *Am J Ophthalmol*. 1981;92(6):799–803.

11. Yang LLH, Lambert SR, Lynn MJ, Stulting RD. Surgical management of glaucoma in infants and children with Peters' anomaly: long-term structural and functional outcome. *Ophthalmology*. 2004;111(1):112–117.

12. Xu BY, Pardeshi AA, Burkemper B, et al. Differences in anterior chamber angle assessments between gonioscopy, EyeCam, and anterior segment OCT: The Chinese American eye study. *Transl Vis Sci Technol*. 2019;8(2):5.

13. He M, Wang D, Jiang Y. Overview of ultrasound biomicroscopy. *J Curr Glaucoma Pract*. 2012;6(1):25–53.

14. Mannino G, Abdolrahimzadeh B, Calafiore S, Anselmi G, Mannino C, Lambiase A. A review of the role of ultrasound biomicroscopy in glaucoma associated with rare diseases of the anterior segment. *Clin Ophthalmol*. 2016;10:1453–1459.

15. Silverman RH. High-resolution ultrasound imaging of the eye–a review. *Clin Exp Ophthalmol*. 2009;37(1):54–67.

16. Safwat AMM, Hammouda LM, El-Zembely HI, Omar IAN. Evaluation of ciliary body by ultrasound bio-microscopy after trans-scleral diode cyclo-photocoagulation in refractory glaucoma. *Eur J Ophthalmol*. 2020;30(6):1335–1341.

17. Pardue MT, Sivak JG. Age- related changes in human ciliary muscle. *Optom Vis Sci*. 2000;77(4):204–210.

18. Ramasubramanian V, Glasser A. Objective measurement of accommodative biometric changes using ultrasound biomicroscopy. *J Cataract Refract Surg*. 2015;41(3):511–526.

19. Qureshi A, Chen H, Saeedi O, et al. Anterior segment ultrasound biomicroscopy image analysis using ImageJ software: intra-observer repeatability and inter-observer agreement. *Int Ophthalmol*. 2019;39(4):829–837.

20. Li J, Drechsler J, Lin A, et al. Repeatability and reliability of quantified ultrasound biomicroscopy image analysis of the ciliary body at the pars plicata. *Ultrasound Med Biol*. 2021;47(7):1949–1956.

21. Ahishakiye E, Van Gijzen MB, Tumwiine J, Wario R, Obungoloch J. A survey on deep learning in medical image reconstruction. *Intell Med*. 2021;1(3):118–127.

22. Islam MT, Aowal MA, Minhaz AT, Ashraf K. Abnormality detection and localization in chest x-rays using deep convolutional neural networks. 2017 arXiv:1705.09850.

23. Ker J, Wang L, Rao J, Lim T. Deep learning applications in medical image analysis. *IEEE Access*. 2018;6, 9375–9389.

24. Litjens G, Kooi T, Bejnordi BE, et al. A survey on deep learning in medical image analysis. *Med Image Anal*. 2017;42, 60–88.

25. Helms RW, Minhaz AT, Wilson DL, Örge FH. Clinical 3D imaging of the anterior segment with ultrasound biomicroscopy. *Transl Vis Sci Technol*. 2021;10(3):11–11.

26. Jamieson RV, Grigg JRB. Chapter 2 - Clinical embryology and development of the eye. In: Hoyt CS, Taylor D, eds. *Pediatric Ophthalmology and Strabismus*. 4th ed. London: W.B. Saunders; 2013;9–15.e1.

27. Kingma DP, Ba J. Adam: a method for stochastic optimization. 3rd International Conference on Learning Representations, ICLR 2015, San Diego, CA, USA, May 7–9, 2015, Conference Track Proceedings; 2015.

28. Volpe NJ. Adler's physiology of the eye: clinical application. *J Neuro-ophthalmol*. 2004;24(4):348.

29. Gupta V, Jha R, Srinivasan G, Dada T, Sihota R. Ultrasound biomicroscopic characteristics of the anterior segment in primary congenital glaucoma. *J Am Assoc Pediatr Ophthalmol Strabismus*. 2007;11(6):546–550.

30. Andrews L, Kueny L, Martinez C, et al. Structural changes of the ciliary body and ciliary processes measured by ultrasound biomicroscopy of primary congenital glaucoma in comparison to glaucoma following congenital cataract surgery. *J Am Assoc Pediatr Ophthalmol Strabismus*. 2019;23(4):e15–e16.

31. Shi Y, Han Y, Xin C, et al. Disease-related and age-related changes of anterior chamber angle structures in patients with primary congenital glaucoma: an in vivo high-frequency ultrasound biomicroscopy-based study. *PLoS One*. 2020;15(1):e0227602.

32. Wu H, Minhaz AT, Helms R, et al. 3D ultrasound biomicroscopy (3D-UBM) imaging and automated 3D assessment of the iridocorneal angle for glaucoma patients. In: *Medical Imaging 2019: Ultrasonic Imaging and Tomography*. Vol. 10955. Bellingham, WA: SPIE; 2019:109550U.